ELSEVIER

Contents lists available at ScienceDirect

Additive Manufacturing

journal homepage: www.elsevier.com/locate/addma





Measuring thermomechanical response of large-format printed polymer composite structures via digital image correlation

Tyler M. Corum a,*, Johnna C. O'Connell a, James C. Brackett A, Ahmed Arabi Hassen b, Chad E. Duty a,b

ARTICLE INFO

Keywords:
Thermoplastic polymer
Short-fiber composites
Digital image correlation
Thermomechanical properties
Microstructure

ABSTRACT

Large-format additive manufacturing (LFAM) is a branch of additive manufacturing (AM) research with the ability to create large structures typically measuring several meters in scale. LFAM is advantageous for tooling applications, not only because it offers the ability to create complex geometries not easily made using subtractive manufacturing processes, but the cost savings of pelletized feedstock used by these systems result in larger parts printed at faster speeds than traditional AM systems. Fiber reinforced polymer (FRP) is a commonly used feedstock material in LFAM structures because it reduces the distortion experienced during printing. However, FRP introduces highly anisotropic thermomechanical properties and contributes to a nonhomogeneous microstructure that can result in critical distortion of dimensions during tooling. Measuring the global thermomechanical response of LFAM structures requires a more representative method that accounts for not only anisotropic properties but also the nonhomogeneous nature of the final part. This is where traditional techniques to measure thermomechanical response, such as thermomechanical analysis (TMA), fall short as they assume homogeneity. This study evaluated the coefficient of thermal expansion (CTE) of LFAM structures as measured by TMA as compared to a novel digital image correlation oven (DIC Oven) system. The LFAM structures were made from 20 % by weight carbon fiber reinforced acrylonitrile butadiene styrene (CF-ABS). TMA measurements showed significant variations in CTE across a single LFAM bead, confirming the need for a global technique that captures overall thermomechanical response. The CTE values measured using the DIC Oven compared well to average TMA values obtained from localized measurements across the sample. The DIC Oven was also used to quantify the effects of different layer orientations on thermomechanical properties, which cannot be easily captured using TMA. A predictive model was also developed by using localized TMA values across an LFAM bead to predict the overall thermomechanical response of an LFAM structure.

1. Introduction

Large-format additive manufacturing (LFAM) is a subset of additive manufacturing (AM) that specializes in printing large volumes (>1 m³) at high deposition rates (~50 kg/hr) [1-7]. Instead of using a wound filament feedstock, LFAM typically uses fiber reinforced polymer (FRP) pellets as feedstock for a single-screw extruder because it reduces the material cost and allows printing of larger parts at faster speeds without the need of a heated build chamber [8,9]. FRPs also typically increase the stiffness and reduce the coefficient of thermal expansion (CTE) exhibited by the print structure after extrusion [1-3,10]. These cost and size advantages make LFAM a popular process for tooling applications

[5,8,9,11]. However, the addition of fiber reinforcement material introduces highly anisotropic thermomechanical properties [12–15] which can cause the composite tool to warp due to thermal distortion that may occur during an autoclave cycle [5,12,16–20]. LFAM tool expansion, as illustrated in Fig. 1, needs to be better understood and allow designers to develop parts that reach correct dimensions after this thermal distortion occurs.

1.1. Non-homogeneity of LFAM structures

While using FRPs does lower the CTE of LFAM structures, the fiber reinforcement also results in nonhomogeneous thermomechanical

Mechanical, Aerospace, and Biomedical Engineering Department, University of Tennessee, Knoxville, TN, USA

b Manufacturing Science Division, Oak Ridge National Laboratory, Oak Ridge, TN, USA

^{*} Correspondence to: University of Tennessee, Knoxville, TN, USA. E-mail address: tcorum2@vols.utk.edu (T.M. Corum).

properties across the structure that are dependent on fiber orientation and dispersion within the matrix material [10,13-15,21-27]. During material extrusion, fibers are aligned in the direction of the print head travel by shear forces acting within the nozzle in a process referred to as fiber alignment that results in a bead with an outer shell of highly aligned fibers and a core of randomly oriented fibers at the center, as shown by Fig. 2 [7,13,14,25,28-31]. The fibers themselves are anisotropic with resistance to thermal expansion significantly higher (over 10x) in the longitudinal direction than transverse [32,33]. This signifies that the orientation of fiber dictates how well the reinforcing material resists thermal expansion. With varying fiber orientation within the bead and thermomechanical properties dependent on fiber orientation, the printed LFAM bead is not only highly anisotropic but also nonhomogeneous across the microstructure. Since an LFAM structure is entirely constructed of these nonhomogeneous beads, the end result is a nonhomogeneous final structure. The hierarchical structure of LFAM prints is illustrated by Fig. 3; namely the microstructure (3 A), the mesostructure (3B), and the macrostructure (3C). The microstructure is the complex arrangement of fiber and porosity within a bead that depends on orientation, distribution, and location along the cross-section. Mesostructure describes how these different beads and layers interact with one another as influenced by microstructure as well as the quality and nature of the interfaces between neighboring beads. The macrostructure refers to the behavior of the printed structure as a whole, including the overarching print geometry and layer sequencing.

1.2. Thermomechanical analysis

The CTE values of a material are an important design consideration in any scenario where a range of temperatures will be experienced. A typical method to measure CTE is by thermomechanical analysis (TMA). TMA is a localized measurement method that analyzes change in dimension as a function of temperature change at a constant rate, typically using a linear variable differential transformer (LVDT). For an anisotropic material, in order to capture the directional dependence of CTE, TMA measurements must be taken in each cardinal direction. While TMA can measure the CTE of homogeneous or orthotropic materials with high accuracy, the technique struggles to accurately measure the properties of a nonhomogeneous material, such as printed FRP, since TMA assumes homogeneity. TMA is also limited by the size of the sample (5 mm×5 mm x 5 mm in this study) which is often smaller than the LFAM bead itself (cross section of 15 mm×6 mm in this study) [1,2, 4,6,34-36]. While multiple TMA measurements can be taken across a sample with varying composition (complex microstructure), it is difficult to capture the interactive effects of the mesostructure that affect the macroscale properties of LFAM structures. Therefore, this study has explored other methods to better represent the macrostructural thermomechanical response of LFAM structures by capturing the effects of complex.

1.3. 2D digital image correlation

A common method for collecting strain data over a large area is digital image correlation. Specifically, two-dimensional digital image

correlation (DIC) is an accurate way to record the strain experienced by a sample by tracking the relative movement of discrete surface markers before and after loading conditions [37-42]. For typical DIC testing, samples are speckled with small black dots against a white background to create a contrast across the desired surface of interest (SOI). This sample SOI is imaged before and after deformation using a camera. The DIC computer software then divides each image into small regions, called subsets, based on the arrangement of speckles to create a unique "fingerprint" across each image. The two-dimensional displacement experienced by the SOI is calculated using DIC computer software by comparing the relative location of corresponding subsets before and after deformation in the form of displacement vectors, as shown by Fig. 4, for each image captured using the camera. By averaging displacement vectors from each image, the DIC software determines the average two-dimensional strain experienced by the sample [39,40]. Thus, DIC can be applied to entire faces of nonhomogeneous samples to capture spatially varying global effects rather than relying on the limited sampling volume available to TMA techniques.

1.4. Digital image correlation oven

The Digital Image Correlation Oven (DIC Oven) shown by Fig. 5 is a novel system that uses DIC to track the strain experienced by an LFAM structure before and after a thermally-induced distortion [24,34,35, 43-45]. The 5MP (megapixel) camera used in this system is mounted under the oven furnace with the sample placed over the opening of a stationary tray. This specific placement of the sample limits strain to a two-dimensional plane that is parallel to and maintains a constant distance from the DIC camera. With the strain calculated by the DIC software and known thermal conditions before and after loading, the global CTE experienced by LFAM structure can be calculated. This system has been optimized and calibrated to provide accurate CTE results within 20 ppm (parts per million) [45]. The DIC Oven is thus advantageous for measuring the CTE of LFAM structures because large surface areas (45 mm×45 mm) can be measured simultaneously to capture the combined effects of both the microstructure and mesostructure on the macroscopic properties.

1.5. Modeling thermally-induced distortion

A model has also been developed as a means of predicting the global response of a large nonhomogeneous structure to thermally-induced strain by combining discrete, localized TMA measurements. Other studies have predicted the thermal response of LFAM structures using finite element analysis (FEA) methods [12,29,44,46,47], but each of these studies make some degree of a simplifying assumption either by averaging TMA samples of dissimilar microstructure or by assuming microstructural symmetry about the bead center. This study addressed the challenge in better representing the complex microstructure, as discussed in Section 1.1, by using a unique TMA sampling method that accounts for site-specific fiber orientation to capture localized microstructural effects to better represent the resulting macrostructural properties

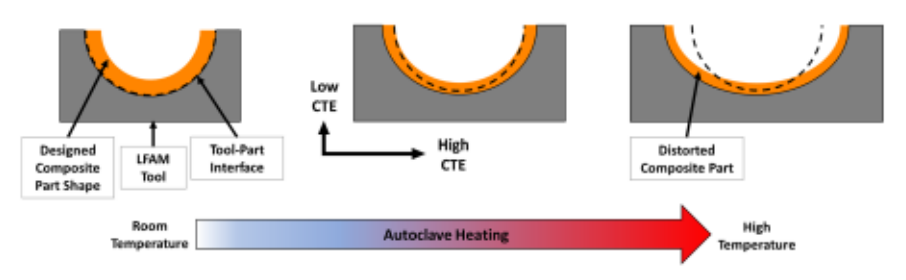


Fig. 1. Composite part distortion from anisotropic thermal expansion is shown.

Fig. 2. The schematic shows fiber alignment as a result of nozzle shearing.

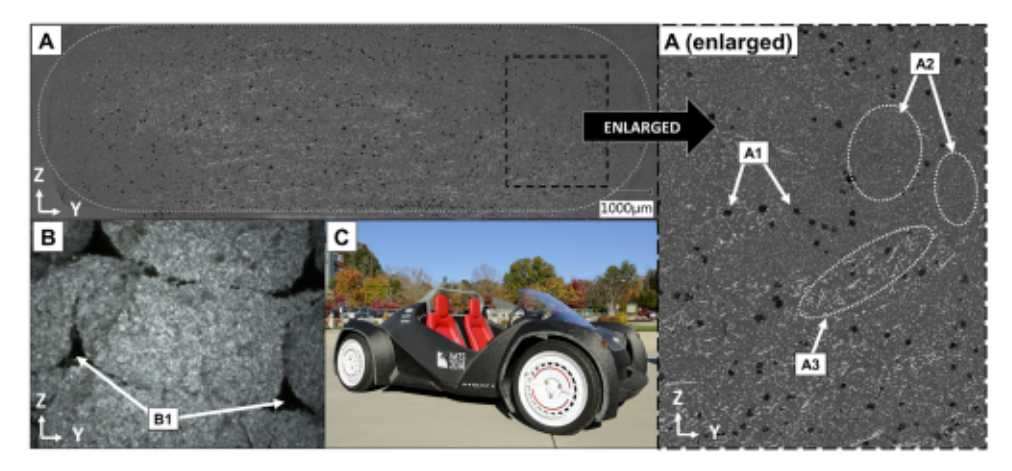


Fig. 3. The hierarchical structure of LFAM are shown as microstructure (A), mesostructure (B), and macrostructure (C) with specific print artifacts of internal voids (A1), highly aligned fiber (A2), randomly oriented fiber (A3), and interbead voids (B1).

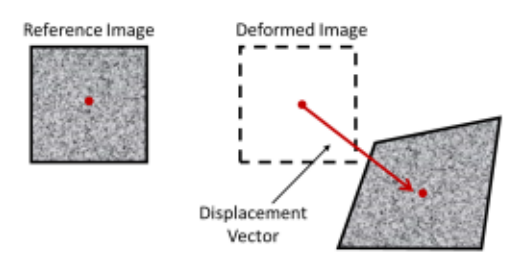


Fig. 4. Subset tracking of a speckled DIC sample (Inspired from [40,41]).

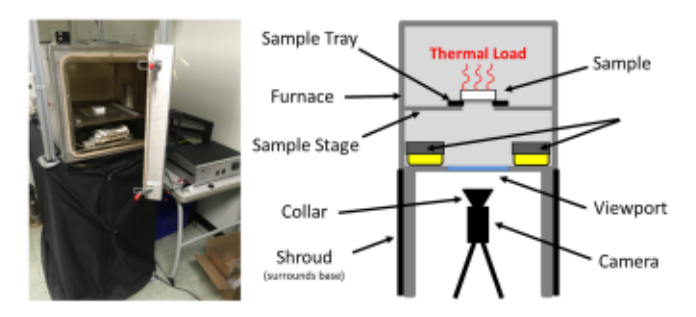


Fig. 5. An image of the DIC Oven (left) and a schematic of major components (right).

2. Materials & experimental methods

This study utilized 20 % by weight carbon fiber reinforced acrylonitrile butadiene styrene (CF-ABS) samples printed on the Big Area Additive Manufacturing (BAAM) system at Oak Ridge National Laboratory [1-5]. The coordinate system used for this work defined the x-direction parallel to the print direction, the y-direction perpendicular to print direction within the printed layer, and the z-direction perpendicular to the build surface. The thermal response was measured in each of these directions using both TMA and the DIC Oven. A TMA sampling technique is described that attempted to capture the complex microstructure of the structure by measuring multiple locations across the LFAM bead. The DIC Oven was used to more accurately represent LFAM properties with global data rather than localized data. Finally, the development of an FEA model within Abaqus is described that utilized the localized TMA measurements to predict mesostructural properties.

2.1. LFAM printing

The BAAM samples tested in this study were printed using CF-ABS with a 12.7 mm diameter nozzle, resulting in beads with an approximate cross-section of 15 mm×6 mm. The final printed structure was machined into a 50 mm×50 mm×50 mm cube with flat, parallel faces. Two different layer orientations were tested in this study to explore the capabilities of the DIC Oven with one sample printed using 0°/0° (0–0) and another using 0°/90° (0–90) layer orientation. A layer orientation of 0–0 has each layer oriented the same direction, whereas a 0–90 layer orientation has each xy-plane rotated 90° from the previous layer, as shown by Fig. 6A. The samples of this work were printed using a "serpentine" toolpath for each layer, where the direction of printing alternates as shown by Fig. 6B.

2.2. TMA approach

Since the orientation and distribution of reinforcing fibers vary considerably across an LFAM bead, as shown previously by Fig. 3A, precision must be taken when using TMA sampling to accurately capture such effects or when developing a predictive model of global behavior. This approach involves taking samples at multiple locations across the bead to capture distinct regions of fiber orientation that have been identified by previous studies that addressed the non-homogenous distribution of fiber orientation across a single LFAM bead [7,14,25,28,48,49]. The TMA samples in this study were taken from a machined LFAM printed structure, as shown in Fig. 7. The LFAM bead was divided into

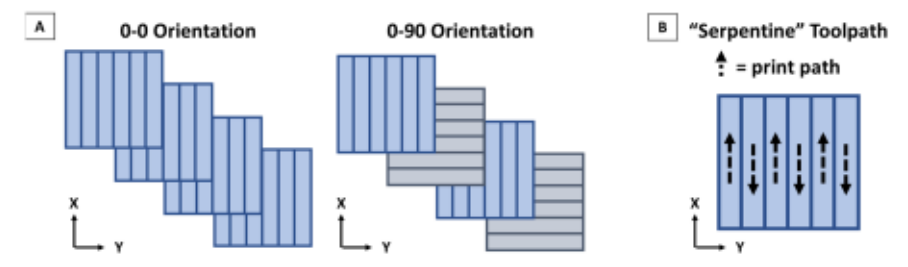


Fig. 6. The layer orientation used to print the 0-0 and 0-90 structures (A) as well as the serpentine toolpath for each layer (B).

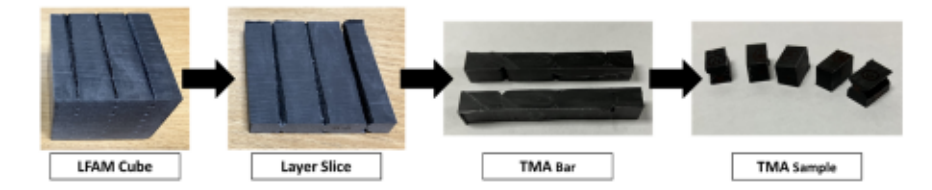


Fig. 7. The process of machining the 50 mm×50 mm x 50 mm LFAM cube to 5 mm×5 mm×5 mm TMA samples.

different regions as shown in Fig. 8, referred to as: left bead interface (LBI), left of center (LC), center of bead (CB), right of center (RC), and right bead interface (RBI). This approach intentionally isolated the highly aligned edges of an LFAM bead while also capturing the interface created by neighboring beads (LBI, RBI), the less aligned off-center region (LC, RC), and the randomly oriented center of the bead (CB). The sampling was accomplished by machining away an individual layer (xy-plane) from an LFAM structure and using a Buehler IsoMet diamond saw to create small (5 mm×5 mm×5 mm) TMA samples with parallel faces (Fig. 7).

The 5 mm×5 mm x 5 mm samples cut from the original LFAM structure were dried in a furnace at 80 °C for at least 8 h, allowed to cool to ambient temperature in a desiccator for at least 2 h, and tested using a TA Instruments Q400 TMA. These dimensions were chosen to complement the size of the 7.5 mm diameter LVDT probe and reduce the influence of probe placement on sample measurement. Each of the CF-ABS TMA samples were tested twice to ensure consistency. Each test consisted of 4 cycles where each cycle heated the sample from room temperature to 90 °C at a rate of 5 °C/min and allowed the sample to naturally cool between cycles. Data was processed using TA Instruments Universal Analysis software where the first set of data was discarded as relieving residual stress. The data from cycles 2-4 were used to calculate CTE values by using the alpha fit function of the TA Universal Analysis software to analyze the mostly linear region from 30 °C to 90 °C. The CTE values from cycles 2-4 were averaged from both tests to determine an average CTE value to represent each TMA sampling location. This process was repeated for the x, y, and z-direction of each TMA sample to calculate an anisotropic CTE for each region and a corresponding standard deviation. Average CTE values recorded using TMA were plotted \pm

one standard deviation.

2.3. DIC oven approach

Both the 0-0 and 0-90 layer orientation CF-ABS cubes were dried in a furnace at 80 °C for at least 8 h and allowed to cool to ambient temperature in a desiccator for at least 2 h. Each cube had an xy- and xz-plane selected for sample preparation based on having minimal defects and the most parallel faces [34,37,39,45]. Each face of interest was lightly coated using white matte finish Krylon High Temperature spray paint to create a light color over the naturally dark CF-ABS surface. Samples were then speckled using a Correlated Solutions Speckle Kit with a stamp, evenly covered in 0.007" sized dots and black ink. This speckling method provided adequate contrast for accurate subset tracking without negatively influencing the face of interest as described in [45]. The contrast of black speckles over a white surface allowed the DIC to measure surface movement by subset tracking [40,41]. The speckled CF-ABS samples tested using the DIC Oven are shown by Fig. 9.

DIC Oven testing began by aligning the x-direction of sample parallel to the x-direction of the Vic Snap-8 software and adjusting the brightness of the oven lighting according to previous work [45]. With the sample properly placed and lighting adjusted, a set of 45 images were taken at room temperature (~20 °C) with an acquisition interval of 100 ms across a 5 s time frame. The DIC Oven furnace was then heated to 90 °C at a rate of 5 °C/min and the sample was allowed to reach thermal equilibrium for at least 6 h to ensure adequate steady state had been reached based on the study in [34]. Once the sample was allowed to reach steady state, a set of 45 images were taken using the same camera conditions as at room temperature to sufficiently capture the

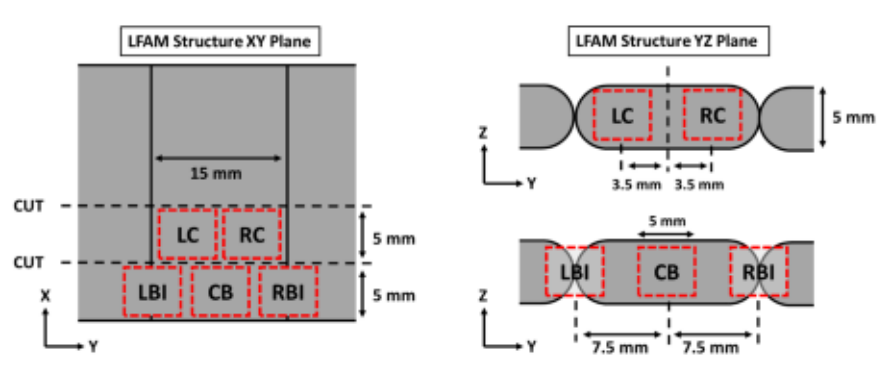


Fig. 8. The cut locations for the LFAM structure to create TMA samples (red).

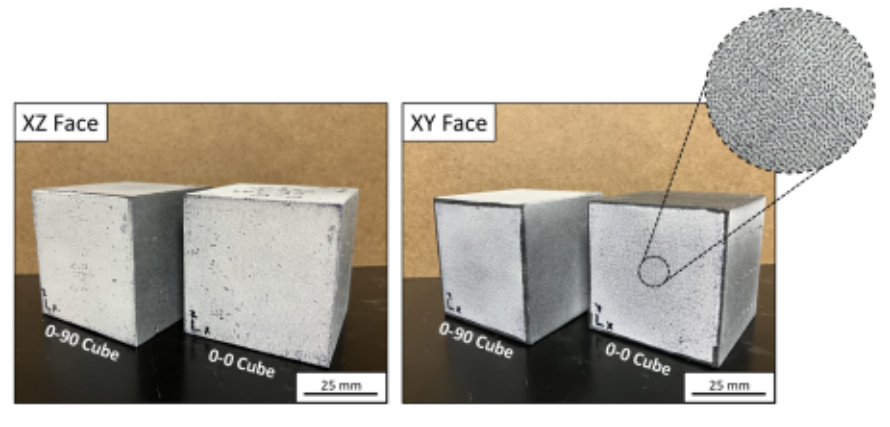


Fig. 9. Speckled LFAM samples that were measured using DIC Oven testing in this study.

thermally-induced strain experienced by the LFAM sample [45]. The total set of 90 images from the room temperature and steady state captures were uploaded to Correlated Solution's Vic-2D software to calculate the average strain experienced by the sample once the thermal load was applied and steady state was reached. Any strain measured at room temperature conditions was treated as system noise and disregarded since no thermal loading had yet occurred. Eq. 1 was used to calculate CTE using known values of: strain at room temperature (ε_{RT}), strain at steady state (ε_{SS}), room temperature (T_{RT}), and steady state temperature (T_{SS}).

$$CTB = \frac{\varepsilon_{SS} - \varepsilon_{RT}}{T_{SS} - T_{RT}}$$
(1)

Bach sample was then run a second time with the orientation rotated 90° so that the x-direction of the physical sample was perpendicular to the x-direction of the software. Averaging the "flipped" orientation measurement with the original measurement accounted for any bias that may result from the alignment and lighting process [34,45]. This test process was run twice for each speckled face of interest resulting in four CTE data points for each directionally dependent value of each face. Corresponding CTE values were averaged to obtain an overall CTE value and standard deviation to represent each cardinal direction for each sample.

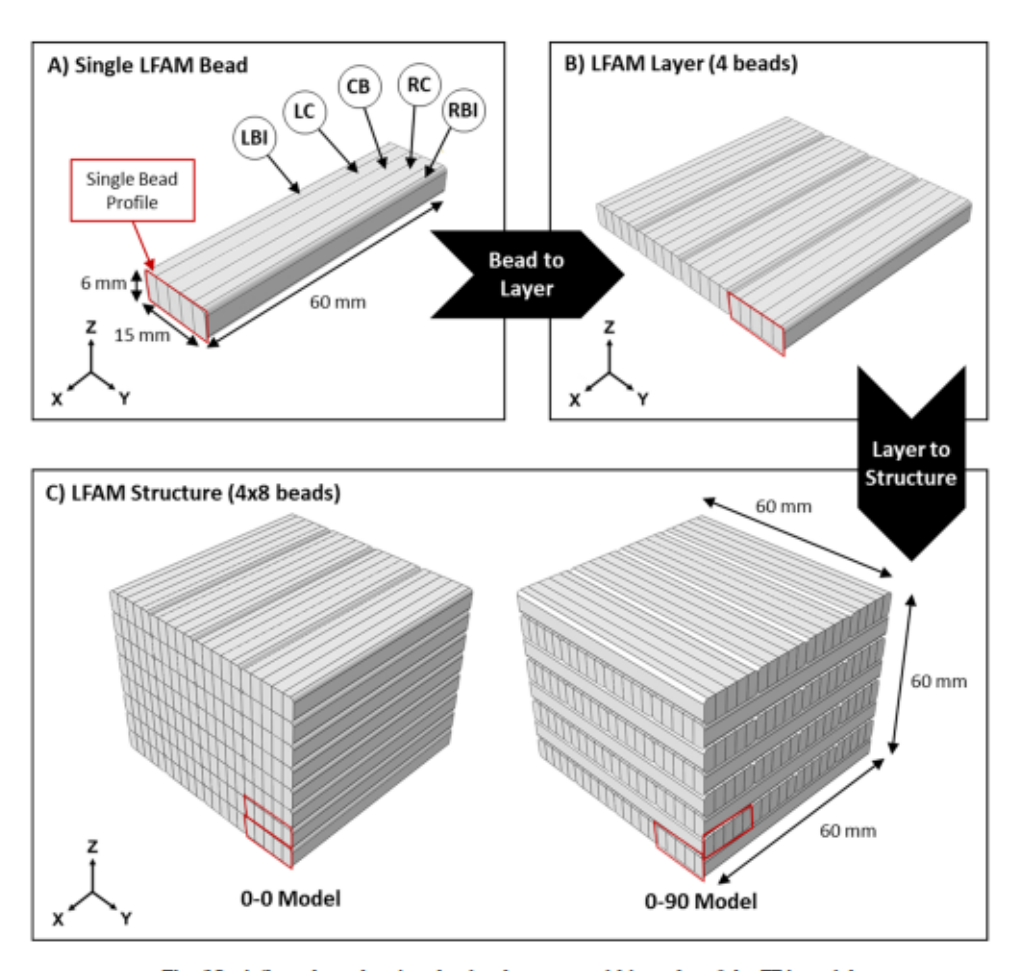


Fig. 10. A flow chart showing the development and hierarchy of the FEA model.

2.4. FEA modeling approach

An FEA model was developed using Abaqus (version 6.18-1) to predict thermomechanical response for both the 0-0 and 0-90 LFAM structure. This model utilized a technique that attempted to capture the effects of varying fiber orientation by implementing localized CTE values to predict more realistic behavior of a fiber reinforced bead. Bach model began with a single LFAM bead comprised of five regions, as shown in Fig. 10A, that corresponded to TMA sampling locations described in Section 2.2. The CTE values assigned to each region in the FEA model were thus representative of the x, y, and z-direction CTE values obtained during TMA testing, as detailed in Table 1. The remaining anisotropic material property inputs for the FEA model were taken from previous LFAM studies that used CF-ABS material and are listed in Table A1 of the appendix [13,46].

Once the multi-material bead was created, successive beads were combined into layers that reflected the serpentine toolpath taken during the printing. A layer was assembled by patterning an LFAM bead along the y-direction to create a 4-bead wide layer, as shown in Fig. 10B. The second and fourth beads of the layer were rotated 180° about the x-axis to capture the effects of the serpentine toolpath on thermomechanical response and resulted in mirrored regions about every other bead interface. For the 0-90 model, the x and y-direction CTE values were switched for every other layer to match layer-specific properties to the global coordinate system used by Abaqus. A merge feature was used to combine individual bead geometries into a single layer so the entire part (now a single LFAM layer) would deform together rather than the deformation of individual beads. With the serpentine patterned LFAM layers completed, successive layers were constructed into cubes by patterning layers along the z-direction to create an 8-layer high LFAM structure. For the 0-90 model, every other layer was rotated 90° to reflect the 0-90 layer orientation of the printed structure. Fig. 10C shows the full multi-bead LFAM cube that was constructed for both the 0-0 and 0-90 structure. Once the correct layers were in place for each model, the merge function was used once again to allow each LFAM structure to deform as a single part, rather than independent layers.

With final dimensions of 60 mm×60 mm x 60 mm for each LFAM structure, a single corner was fixed in x, y, and z-directions to allow each model to expand from a single reference point. The LFAM structures were each thermally loaded by creating a change in temperature of 70 °C to simulate thermal loading from room temperature (20 °C) to a heated temperature of 90 °C throughout each structure. A mesh was created across each structure using 15900 total 3D stress elements with cubic shape and an element size of 3 mm×3 mm x 3 mm. The element type implemented in each model was an 8-node thermally coupled trilinear displacement element (C3D8T element type).

3. Experimental results and discussion

3.1. TMA results

The average CTE values measured using TMA, based on the sampling location described in Section 2.2, are displayed in Table 1 with ± one standard deviation listed in parentheses for the 0–0 orientation CF-ABS sample. Fig. 11 also shows the CTE results plotted with standard

Table 1
CTE values recorded from TMA testing.

Relative Position	Region	x-direction	y-direction	s-direction
-7.5 mm	LBI	18.9 (± 1.4)	81.6 (± 9.7)	81.1 (± 3.1)
-3.5 mm	LC	$23.9 (\pm 4.0)$	$74.6 (\pm 1.0)$	113.6 (± 4.1)
0.0 mm	CB	$13.0 (\pm 0.5)$	$35.9 (\pm 2.0)$	$123.8 (\pm 6.2)$
3.5 mm	RC	$14.8 (\pm 2.2)$	$65.1 (\pm 1.0)$	$100.9 (\pm 7.3)$
7.5 mm	RBI	16.3 (± 4.1)	46.6 (± 3.3)	$114.7 (\pm 4.0)$

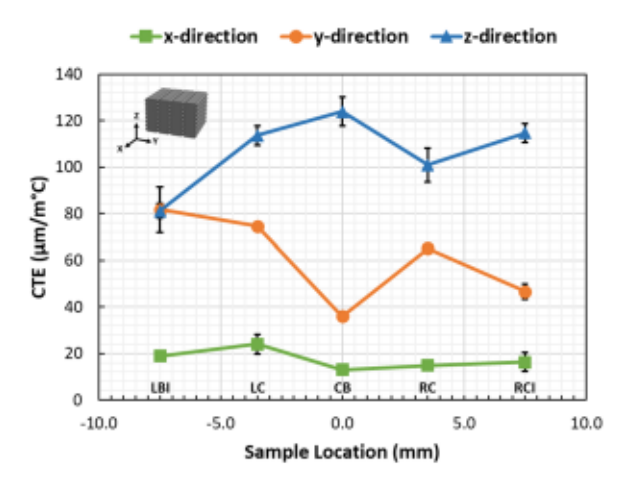


Fig. 11. CTE values of the 0-0 CF-ABS cube taken using TMA testing.

deviation bars to show variation across the printed bead with the CB identified at 0.0 mm. Overall, the trend of the TMA data shows an increase in CTE values from the x-direction to y-direction with z-direction being the highest value. This trend was expected not only due to the anisotropic response of the fiber reinforced material, but also based on the nonhomogeneous distribution of fiber orientation throughout an LFAM printed bead, commonly referred to as the highly oriented shell and randomly oriented core [7,14,25,28,32,48,49]. Note that due to the stochastic nature of shear fiber alignment, there remains a fair degree of orientation variability even in the highly aligned regions. However, the majority of fibers shear-align in the direction of the print (x-direction), so the x-direction CTE (CTEx) values were lowest at each region tested since the fibers best resist thermal expansion in the longitudinal direction. The y-direction CTE (CTE_v) values were higher because the expansion was measured perpendicular to the direction of the highly aligned fiber where less resistance to thermal expansion was provided by the fiber reinforcement. The z-direction CTE (CTEz) values were highest not only because less resistance to expansion was offered transverse to the highly oriented fiber regions but also from effects of the tamper used by BAAM to "squish" the bead that further decreased the amount of fiber oriented parallel to the z-direction [1,7,28]. This variation of CTE values exhibited across the bead are a function of varying fiber orientation and emphasizes the importance of precise sampling techniques across multiple locations.

Notice the CTE data is not symmetric about the center of the bead. While the LC and RC regions of the bead are similar, the CTEx, CTEv, and CTE, values of RC were all lower. The LBI and RBI regions differ the most with the CTE_v and CTE_z values of LBI being much more similar than at the right interface. This was most likely a result of the asymmetrical shear field imposed by the reversing deposition of the serpentine toolpath (Fig. 6B) that was used to create the LFAM structure [50]. The serpentine path used during material deposition created contact along one bead edge against already deposited material while the opposite bead edge was free. This affected material flow and introduced an asymmetric shear profile within each bead. Overall, the LC and RC regions are more symmetrical about the CB than the LBI and RBI regions, likely due to effects of the neighboring beads within the layer affecting the bead edge with these effects reduced towards the bead center. Another trend of this data was while CTEx stayed relatively similar across the bead, the CTE_v and CTE_z values changed inversely relative to one another from region to region across the bead position. Specifically analyzing points from CB to RC, as the value of CTEz decreases, the CTEv increases. This trend was consistent across each sampled location with the inverse of this effect also true. This trend quantified the rotation of the fiber orientation tensor and how tensor orientation changed across the bead while maintaining the x, y, and z-relationships described in [7, 28,29,51-53]. This initial TMA data clearly shows the dependence of CTE on bead location and emphasizes the importance of taking multiple samples across a bead to represent the complex microstructure of an LFAM structure described previously in Section 1.1.

3.2 DIC oven results

The CTE values obtained by DIC Oven testing are shown in Table 2 with \pm one standard deviation listed in parentheses for both the 0-0 and 0-90 samples. Results from the 0-0 cube were similar to those obtained using TMA in other studies [14,15]. Like the TMA results, the 0-0 cube exhibited the lowest CTE value in the x-direction and the highest in the z-direction. This was attributed to the effects of fiber orientation since the aligned fibers in the x-direction best resist expansion in the longitudinal direction (also the x or print direction), resulting in lower CTEx. The y-direction saw higher CTE values than CTEx because expansion occurred transversely to the highly aligned fibers, which provided less resistance to expansion. The CTEz value was highest because not only did expansion occur transversely to aligned fiber but also since the bead was printed approximately 2x wider than the layer height (~15 mm width vs. ~ 6 mm layer height). This typical LFAM bead geometry, resulted in over 2x more interfaces between adjacent layers than between adjacent beads in a given distance along the respective direction, meaning there were also over 2x more regions of highly oriented fiber for the xz-plane than the xy-plane. Due to the increased number of highly oriented fiber regions at layer interfaces, the CTEz values were higher than those measured in the y-direction.

The results in Table 2 show that the 0-90 layer orientation had a significant influence on thermomechanical properties as represented by the reduced anisotropy in the xy-plane CTE of the 0-90 cube. Results showed the difference in CTEx and CTEv was reduced from 246 % for the 0-0 cube to only 10 % for the 0-90 cube due to alternating layer expanding perpendicular to each other. Compared to the 0-0 cube, the 0-90 cube exhibited higher CTEx and lower CTEv while CTEz was relatively unaffected by the different layer orientation. These results were attributed to mesostructural effects of the 0-90 layer orientation. While each layer of the 0-0 cube deformed together with little to no resistance from surrounding layers, the 0-90 cube experienced expansion in competing directions from each alternated layer that resulted in a less anisotropic response by the CTEx and CTEv values. Since layer orientation is a mesostructural feature, the effects of the different layer orientation pattern on thermomechanical response were able to be captured with the DIC Oven but were not captured by TMA due to its localized testing nature.

3.3. Comparing TMA and DIC oven results

The results taken from TMA testing were compared to the DIC results to understand how the localized TMA method differed from the global DIC Oven measurements. The plot shown in Fig. 12 compares x, y, and z-direction CTE values taken using the site-specific TMA data with data from the DIC Oven overlaid to represent global CTE values. The CTE_x values obtained were similar for both the TMA and DIC Oven techniques with 3 of 5 TMA locations falling within 10 % of the DIC Oven values. Since the x-direction thermomechanical properties should be consistent along the print within the same extruded bead, it is reasonable that the structure should exhibit similar CTE_x properties. The CTE_y values collected using the DIC Oven were lower than 3 of the 5 TMA values

Table 2 CTE values obtained from DIC Oven testing.

DIC Oven C	DIC Oven CTE Results (µm/m°C)				
Cube	x-direction	y-direction	≰-direction		
0_0	15.3 (± 1.1)	52.9 (± 2.2)	122.2 (± 3.5)		
0-90	26.9 (± 1.4)	29.5 (± 1.1)	119.7 (± 6.0)		

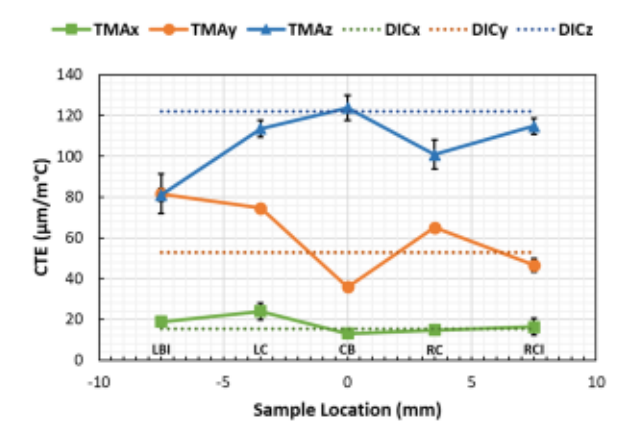


Fig. 12. A comparison of CTE values taken using both TMA and the DIC Oven.

collected. This was likely due to the less accurate representation of the LFAM sample by TMA since the TMA samples could not account for surrounding beads that acted as a boundary condition to limit expansion at a mesostructural scale. Compared to the TMA values, each of the $\rm CTE_z$ values measured via the DIC Oven were higher except those taken from the center. The most likely reason for the discrepancy was the ability of the DIC Oven to capture effects of multiple layers expanding simultaneously while the TMA only measured a small section within a single layer.

TMA did not accurately represent the global response of the LFAM structure because it is not able to capture the influence of the meso-structure on the thermally-induced distortion. Therefore, the DIC Oven demonstrated an ability to more realistically characterize the global response of an LFAM structure without requiring nearly as many tests. For example, the DIC Oven required 4 tests to represent a single LFAM structure, while TMA required over 30 tests to account for the nonhomogeneous, anisotropic thermomechanical response due to the localized nature of TMA.

3.4. FEA model results

Both the 0-0 and 0-90 structures were modeled to show effects of different layer orientation on the predicted thermomechanical response. The average CTE of the model was calculated by averaging directional strain of each element in each direction and dividing by the change in temperature, just as in Eq. 1. Results predicted by the FEA model were compared to the global CTE values as shown in Fig. 13. The DIC Oven results were used to validate the FEA approach.

The FEA results from the 0-0 model were 13-15 % higher than the

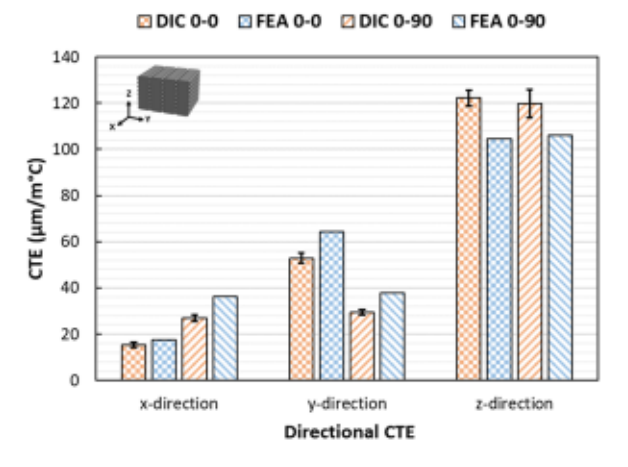


Fig. 13. The CTE results predicted by the FEA model were compared to values recorded by the DIC Oven.

DIC Oven results for x, y, and z-direction and showed promise as a predictive tool not only because they were similar to the DIC Oven results, but also because they followed the same pattern of $\rm CTE_x < \rm CTE_y < \rm CTE_z$ that was exhibited due to fiber orientation. The 0–0 FEA model verified that when site-specific TMA sampling was coupled with the appropriate domain of a bead in the FEA model, TMA could be used as a viable input to predict global response of an LFAM structure.

The 0–90 model captured the effects of layer orientation using the same TMA inputs as the 0–0 model. While the 0–90 model predictions were further elevated (25–35 % higher than the DIC Oven measurements), the concept of predicting global performance based on site-specific properties was validated. The model predicted that anisotropy would be reduced between CTE $_{\rm x}$ and CTE $_{\rm y}$ from 267 % for the 0–0 model to only a 4 % difference for the 0–90 model. It was also observed from both the 0–0 and 0–90 model that the FEA predicted CTE $_{\rm z}$ values were lower than the DIC Oven measured values. While the x- and y-direction thermomechanical properties were primarily compared for effects of layer orientation, CTE $_{\rm z}$ values were underestimated by the FEA modeling since the mesostructural effects of multiple layers expanding in the z-direction were not adequately captured by TMA.

Initial FEA results showed that with precise sampling of bead material, this FEA model was a valid approach to predict thermally-induced distortion. The differences between modeled and measured results suggest that a modified technique to collect smaller TMA samples may improve the predicted CTE values, especially for those measured along the z-direction to capture fiber orientation localized at layer interfaces. A correction factor may also be developed and implemented in future studies to more accurately predict CTE values, but more work in this area is required.

4. Conclusions

This study demonstrated a new method (the DIC Oven) for measuring the thermal response of structures created via LFAM from FRP materials and validated the global properties of an LFAM structure using site-specific TMA measurements. Precise TMA sampling at prescribed locations across the bead showed a clear variation in thermomechanical properties (CTE) and highlighted the inability of TMA to provide a single point characterization of such a nonhomogeneous structure. By contrast, the DIC Oven captured global, anisotropic CTE values that better represented the performance of the overall LFAM structure, especially for applications such as printed tooling. Results from the DIC Oven compared well to the average data measured across the sample using TMA. While the majority of CTE_x values measured by TMA fell within 10 % of the DIC Oven values, the CTE_v and CTE_z values from TMA varied considerably from the global DIC Oven results due to site specific fiber orientation. The difference in localized TMA values from those measured by the DIC Oven were attributed to limitations of TMA to handle variations at the microstructural scale and reinforced the

need for global measurements offered by the DIC Oven.

To quantify the global effects of different layer orientations (mesostructural variations) on thermomechanical properties, the DIC Oven was used to measure a cube printed using 0–0 and 0–90 layer orientations. Results from the DIC Oven showed the anisotropic response exhibited by xy-plane CTE values was reduced from 246 % to only 10 % due to the counteractive effects of alternating layers that preferentially expanded perpendicular to each other.

A predictive FEA model was also developed to simulate thermal distortion of LFAM structures and showed promising initial results with patterns of anisotropy similar to those measured using the DIC Oven. FEA predictions also properly captured the effects of layer orientation on the thermomechanical response, showing a similar reduction in anisotropy for xy-plane CTE values when comparing the 0–0 and 0–90 models. These FEA predictions suggest that, with further refinements and validation using the DIC Oven, a model can be developed to accurately predict thermally-induced distortion of an LFAM structure with mesostructural variations. Future work includes the further development of a predictive FEA model and investigation into the relationship between fiber orientation and thermomechanical properties using the DIC Oven.

CRediT authorship contribution statement

Chad E. Duty: Writing – review & editing, Supervision, Resources, Methodology, Funding acquisition, Conceptualization. Ahmed Arabi Hassen: Supervision, Resources, Funding acquisition, Conceptualization. James C. Brackett: Writing – review & editing, Methodology, Investigation. Johnna C. O'Connell: Validation, Investigation, Data curation. Tyler M. Corum: Writing – review & editing, Writing – original draft, Validation, Supervision, Software, Project administration, Methodology, Investigation, Formal analysis, Data curation, Conceptualization.

Declaration of Competing Interest

The authors declare that they have no known competing financial interests or personal relationships that could have appeared to influence the work reported in this paper.

Acknowledgements

This research was funded by the Southeastern Advanced Machine Tools Network (SEAMTN) through the U.S. Department of Defense, Defense Manufacturing Community Support Program, under Grant No. MCS1940-21-01. This study was also sponsored by the U.S. Department of Energy, Office of Energy Efficiency and Renewable Energy, Advanced Manufacturing Office, under contract DE-AC05-00OR22725 with UT-Battelle, LLC and partially supported by the National Science Foundation under Grant No. 2055529.

Appendix A

Table A1Anisotropic material property inputs used for the Abaqus model.

Material Property	Direction	Value	Units
Density	_	1076	Kg/m ³
Specific Heat	_	1408	J/kgK
Thermal Conductivity	λ_1	1.284	W/mK
	λ_2	0.5522	W/mK
	λ_3	0.2337	W/mK
Elastic Modulus	E11	6158	MPa
	E22	2845	MPa

Table A1 (continued)

Material Property	Direction	Value	Units
	E33	1244	MPa
Shear Modulus	G12	741	MPa
	G13	431	MPa
	G23	426	MPa
Poisson's Ratio	v12	0.23	_
	v23	0.37	_
	v13	0.32	_

Data Availability

Data will be made available on request.

References

- C.E. Duty, V. Kunc, B. Compton, B. Post, D. Erdman, R. Smith, R. Lind, P. Lloyd, L. Love, Structure and mechanical behavior of Big Area Additive Manufacturing (BAAM) materials, Rapid Prototyp. J. 23 (2017) 181–189, https://doi.org/ 10.1108/RPJ-12-2015-0183.
- [2] C.E. Duty, T. Drye, A. Franc, Material Development for Tooling Applications Using Big Area Additive Manufacturing (BAAM), 2015. https://doi.org/10.2172/ 1209207
- [3] C. Duty, C. Ajinjeru, V. Kishore, B. Compton, N. Hmeidat, X. Chen, P. Liu, A. Hassen, J. Lindahl, V. Kunc, A. VISCOELASTIC Model for evaluating extrusion-based print conditions, in: Proc. 28th Annu. Int. SOLID Free. Fabr. Symp. 2022 Addit. Manuf. Conf., 2017: p. 12. (https://hdl.handle.net/2152/89854).
- [4] C. Duty, C. Ajinjeru, V. Kishore, B. Compton, N. Hmeidat, X. Chen, P. Liu, A. A. Hassen, J. Lindahl, V. Kunc, What makes a material printable? A viscoelastic model for extrusion-based 3D printing of polymers, J. Manuf. Process. 35 (2018) 526–537, https://doi.org/10.1016/j.jmapro.2018.08.008.
- [5] A.A. Hassen, J. Lindahl, sun, B. Post, L. Love, V. Kunc, Additive manufacturing of composite tooling using high temperature thermoplastic materials, in: SAMPE Conf. Proc., Long Beach, CA, 2016: p. 11.
- [6] J. Brackett, Y. Yan, D. Cauthen, V. Kishore, J. Lindahl, T. Smith, Z. Sudbury, H. Ning, V. Kunc, C. Duty, Characterizing material transitions in large-scale additive manufacturing, Addit. Manuf. 38 (2021) 101750, https://doi.org/ 10.1016/j.addma.2020.101750.
- [7] P. Pibulchinda, E. Barocio, A.J. Favaloro, R.B. Pipes, Influence of printing conditions on the extrudate shape and fiber orientation in extrusion deposition additive manufacturing, Compos. Part B Eng. 261 (2023) 110793, https://doi.org/ 10.1016/j.compositesb. 2023.110793
- [8] B.K. Post, R.F. Lind, P.D. Lloyd, V. Kunc, J.M. Linhal, L.J. Love, The Economics of Big Area Additive Manufacturing, in: Proc. 26th Annu. Int. Solid Free. Fabr. Symp. – Addit. Manuf. Conf., 2016: p. 7.
- [9] B. Post, B. Richardson, R. Lind, L.J. Love, P. Lloyd, V. Kunc, B.J. Rhyne, A. Roschli, J. Hannan, S. Nolet, K. Veloso, P. Kurup, T. Remo, D. Jenne, Big area additive manufacturing application in wind turbine molds, in: Proc. 28th Annu. Int. Solid Free. Fabr. Symp. Addit. Manuf. Conf., 2017: p. 17. https://doi.org/10.26153/tsw/16964.
- [10] L.J. Love, V. Kunc, O. Rios, C.E. Duty, A.M. Elliott, B.K. Post, R.J. Smith, C.A. Blue, The importance of carbon fiber to polymer additive manufacturing, J. Mater. Res. 29 (2014) 1893–1898, https://doi.org/10.1557/jmr.2014.212.
- [11] V. Kunc, A.A. Hassen, J. Lindahl, S. Kim, B. Post, L. Love, Large scale additively manufactured tooling for composites, in: SAMPE Symp. Exhib. 2017 Proc., 2017.
- [12] A. Hassen, A. Lambert, J. Lindahl, D. Hoskins, C. Duty, S. Simunovic, C. Chin, V. Oancea, L. Love, Simulation Assisted Design for an Additively Manufactured Autoclave Tool Accounting for an Anisotropic Expansion, in: CAMX 2019, NA SAMPE, 2019. https://doi.org/10.33599/nasampe/c.19.0858.
- [13] A.A. Hassen, R.B. Dinwiddie, S. Kim, H.L. Tekinap, V. Kumar, J. Lindahl, P. Yeole, C. Duty, U. Vaidya, H. Wang, V. Kunc, Anisotropic thermal behavior of extrusion-based large scale additively manufactured carbon-fiber reinforced thermoplastic structures, Polym. Compos. 43 (2022) 3678–3690, https://doi.org/10.1002/psg.36645.
- [14] J.L. Colón Quintana, L. Slattery, J. Pinkham, J. Keaton, R.A. Lopez-Anido, K. Sharp, Effects of fiber orientation on the coefficient of thermal expansion of fiber-filled polymer systems in large format polymer extrusion-based additive manufacturing, Materials 15 (2022) 2764, https://doi.org/10.3390/ma15082764.
- [15] K.M.M. Billah, F.A.R. Lorenzana, N.L. Martinez, R.B. Wicker, D. Espalin, Thermomechanical characterization of short carbon fiber and short glass fiberreinforced ABS used in large format additive manufacturing, Addit. Manuf. 35 (2020) 101299, https://doi.org/10.1016/j.addma.2020.101299.
- [16] D.E. Bowles, S.S. Tompkins, Prediction of coefficients of thermal expansion for unidirectional composites, J. Compos. Mater. 23 (1989) 370–388, https://doi.org/ 10.1177/002199838902300405
- [17] G. Twigg, A. Poursartip, G. Fernlund, Tool–part interaction in composites processing. Part I: experimental investigation and analytical model, Compos. Part Appl. Sci. Manuf. 35 (2004) 121–133, https://doi.org/10.1016/S1359-835X(03) 00131-3.

- [18] X. Zeng, J. Raghavan, Role of tool-part interaction in process-induced warpage of autoclave-manufactured composite structures, Compos. Part Appl. Sci. Manuf. 41 (2010) 1174–1183, https://doi.org/10.1016/j.compositesa.2010.04.017.
- [19] P. Yeole, C. Herring, A. Hassen, V. Kunc, R. Stratton, U. Vaidya, Improve durability and surface quality of additively manufactured molds using carbon fiber prepreg, Polym. Compos. 42 (2021) 2101–2111, https://doi.org/10.1002/pc.25962.
- [20] P. Roozbehjavan, B. Tavakol, A. Ahmed, H. Koushyar, R. Das, R. Joven, B. Minaie, Experimental and numerical study of distortion in flat, L-shaped, and U-shaped carbon fiber-epoxy composite parts, J. Appl. Polym. Sci. 131 (2014), https://doi. org/10.1002/app.40439.
- [21] G. Marom, A. Weinberg, The effect of the fibre critical length on the thermal expansion of composite materials, J. Mater. Sci. 10 (1975) 1005–1010, https://doi. org/10.1007/BF00823217.
- [22] H.L. Tekinalp, V. Kunc, G.M. Velez-Garcia, C.E. Duty, L.J. Love, A.K. Naskar, C. A. Blue, S. Ozcan, Highly oriented carbon fiber–polymer composites via additive manufacturing, Compos. Sci. Technol. 105 (2014) 144–150, https://doi.org/10.1016/j.compscitech.2014.10.009.
- [23] D. Jiang, D.E. Smith, Anisotropic mechanical properties of oriented carbon fiber filled polymer composites produced with fused filament fabrication, Addit. Manuf. 18 (2017) 84–94, https://doi.org/10.1016/j.addma.2017.08.006.
- [24] R. Walker, M. Korey, A.M. Hubbard, C.M. Clarkson, T. Corum, T. Smith, C. J. Hershey, J. Lindahl, S. Ozcan, C. Duty, Recycling of CF-ABS machining waste for large format additive manufacturing, Compos. Part B Eng. 275 (2024) 111291, https://doi.org/10.1016/j.compositesb.2024.111291.
- [25] N. Sayah, D.E. Smith, Correlation of microstructural features within short carbon Fiber/ABS manufactured via large-area additive- manufacturing beads, J. Compos. Sci. 8 (2024) 246, https://doi.org/10.3390/jcs8070246.
- [26] N. Sayah, D.E. Smith, Effect of process parameters on void distribution, volume fraction, and sphericity within the bead microstructure of large-area additive manufacturing polymer composites, Polymers 14 (2022) 5107, https://doi.org/ 10.3390/polym14235107.
- [27] Z. Wang, D.E. Smith, Numerical analysis of screw swirling effects on fiber orientation in large area additive manufacturing polymer composite deposition, Compos. Part B Eng. 177 (2019) 107284, https://doi.org/10.1016/j. compositesb.2019.107284.
- [28] B. Šeta, M. Sandberg, M. Brander, M.T. Mollah, D. Pokkalla, V. Kumar, J. Spangenberg, Modeling fiber orientation and strand shape morphology in threedimensional material extrusion additive manufacturing, Compos. Part B Eng. (2023) 110957, https://doi.org/10.1016/j.compositesb.2023.110957.
- [29] T. Rusell, D. Jack, Initial fiber orientation effects on predicting thermo-mechanical properties of large volume, Fused Filam. Compos. 10 (2018).
- [30] S.-Y. Fu, B. Lauke, E. Mäder, C.-Y. Yue, X. Hu, Tensile properties of short-glass-fiber- and short-carbon-fiber-reinforced polypropylene composites, Compos. Part Appl. Sci. Manuf. 31 (2000) 1117–1125, https://doi.org/10.1016/S1359-835X(00) 00068.3
- [31] D. Hoskins, C. Ajinjeru, V. Kunc, J. Lindahl, D.M. Nieto, C. Duty, The Effect of Shear-Induced Fiber Alignment on Viscosity for 3D Printing of Reinforced Polymers, (n.d.).
- [32] I.M. Daniel, O. Ishai, Engineering Mechanics of Composite Materials, 2nd ed., Oxford Univ. Press, New York, NY, 2006.
- [33] P.K. Mallick, Fiber-Reinforced Composites: Materials, Manufacturing, and Design, 3rd ed., [expanded and rev. ed.], CRC Press, Boca Raton, FL, 2008.
- [34] T.M. Corum, J.C. O'Connell, A.A. Hassen, C.E. Duty, Measuring Thermally-Induced Distortion of Large-Scale Composite Printed Structures Using Digital Image Correlation, in: SAMPE Conf. Proc., Society for the Advancement of Material and Process Engineering - North America, Seattle, WA, 2023: p. 15. https://doi.org/ 10.33599/nasampe/s.23.0098.
- [35] T. Corum, J. O'Connell, M. Heres, J. Foote, C. Duty, Characterizing thermomechanical properties of large-format printed composite polymer structures, in: Proc. 34th Annu. Int. SOLID Free. Fabr. Symp. 2023 – Addit. Manuf. Conf., Austin, TX, 2023: p. 9. https://doi.org/10.26153/tsw/51079.
- [36] E37 Committee, Test Method for Linear Thermal Expansion of Solid Materials by Thermomechanical Analysis, ASTM International, n.d. https://doi.org/10.1520/ E0831-19.
- [37] T.C. Chu, W.F. Ranson, M.A. Sutton, Applications of digital-image-correlation techniques to experimental mechanics, Exp. Mech. 25 (1985) 232–244, https://doi.org/10.1007/BF02325092.
- [38] J.S. Lyons, J. Liu, M.A. Sutton, High-temperature deformation measurements using digital-image correlation, Exp. Mech. 36 (1996) 64–70, https://doi.org/10.1007/ BF02328699.

- [39] P. Bing, X. Hui-min, H. Tao, A. Asundi, Measurement of coefficient of thermal expansion of films using digital image correlation method, Polym. Test. 28 (2009) 75–83, https://doi.org/10.1016/j.polymertesting.2008.11.004.
- [40] P. Bing, H. Xie, Z. Wang, K. Qian, Z. Wang, Study on subset size selection in digital image correlation for speckle patterns, Opt. Express 16 (2008) 7037, https://doi. org/10.1364/OE.16.007037.
- [41] P. Bing, K. Qian, H. Xie, A. Asundi, Two-dimensional digital image correlation for in-plane displacement and strain measurement: a review, Meas. Sci. Technol. 20 (2009) 062001, https://doi.org/10.1088/0957-0233/20/6/062001.
- [42] R. Spencer, S. Álwekar, E. Jo, A.A. Hassen, S. Kim, U. Vaidya, Fiber orientation evaluation in reinforced composites using digital image correlation and thermal excitation, Compos. Part B Eng. 234 (2022) 109713, https://doi.org/10.1016/j. compositesb.2022.109713.
- [43] D. Hoskins, V. Kunc, A. Hassen, J. Lindahl, C. DutyCharacterizing thermal expansion of large-scale 3D printed parts SAMPE 2019 - Charlotte NC, SAMPE2019, , SAMPE - Charlotte NC, SAMPE201910.33599/nasampe/s.19.1598.
- [44] D. Hoskins, S. Kim, A. Hassen, J. Lindahl, V. Kunc, C. Duty, Modeling thermal expansion of a large area extrusion deposition additively manufactured parts using a non-homogenized approach, in: 2019 International Solid Freeform Fabrication Symposium, Austin, TX, 2019: p. 10. https://doi.org/10.26153/tsw/17350.
- [45] T. Corum, J. O'Connell, J. Brackett, R. Spencer, A. Hassen, C. Duty, Characterizing the Thermal-Induced Distortion of Large-Scale Polymer Composite Printed Structures, in: Proc. 33rd Annu. Int. SOLID Free. Fabr. Symp. 2022 – Addit. Manuf. Conf., Austin, TX, 2022: p. 20. https://doi.org/10.26153/tsw/44338.
- [46] S. Kim, H. Baid, A. Hassen, A. Kumar, J. Lindahl, D. Hoskins, C. Ajinjeru, C. Duty, P. Yeole, U. Vaidya, R. Dinwiddie, F. Abdi, L. Love, S. Simunovic, V. Kunc, Analysis on Part Distortion and Residual Stress in Big Area Additive Manufacturing with Carbon Fiber-Reinforced Thermoplastic using Dehomogenization Technique, in: CAMX 2019, NA SAMPE, 2019. https://doi.org/10.33599/nasampe/c.19.0694.

- [47] V. Kunc, B. Compton, S. Simunovic, C. Duty, L. Love, B. Post, C. Blue, F. Talagani, R. Dutton, C. Godines, S. DorMohammadi, H. Baid, F. AbdiModeling of large scale reinforced polymer additive manufacturing: Antec 2015 Proc. 2015, Antec Proc. 2015.
- [48] N.S. Hmeidat, D.S. Elkins, H.R. Peter, V. Kumar, B.G. Compton, Processing and mechanical characterization of short carbon fiber-reinforced epoxy composites for material extrusion additive manufacturing, Compos. Part B Eng. 223 (2021) 109122, https://doi.org/10.1016/j.compositesb.2021.109122.
- [49] Z. Wang, Z. Fang, Z. Xie, D.E. Smith, A review on microstructural formations of discontinuous fiber-reinforced polymer composites prepared via material extrusion additive manufacturing: fiber orientation, fiber attrition, and micro-voids distribution, Polymers 14 (2022) 4941, https://doi.org/10.3390/polym14224941.
- [50] E.B. Trigg, N.S. Hmeidat, L.M. Smieska, A.R. Woll, B.G. Compton, H. Koerner, Revealing filler morphology in 3D-printed thermoset nanocomposites by scanning microbeam X-ray scattering, Addit. Manuf. 37 (2021) 101729, https://doi.org/ 10.1016/j.addma.2020.101729.
- [51] P. Pibulchinda, E. Barocio, R.B. Pipes, Influence of fiber orientation on deformation of additive manufactured composites, Addit. Manuf. 49 (2022) 102483, https:// doi.org/10.1016/j.addma.2021.102483.
- [52] T.D. Russell, The effects of fiber orientation on stiffness and thermal expansion of large volume, anisotropic, short-fiber, composite material fabricated by fused filament fabrication, Baylor University, 2017. (https://baylor-ir.tdl.org/bitstrea m/handle/2104/10199/RUSSELL-THESIS-2017.pdf?sequence=1&isAllowed=y/ (accessed June 19, 2023).
- [53] Z. Wang, D. Smith, Rheology effects on predicted fiber orientation and elastic properties in large scale polymer composite additive manufacturing, J. Compos. Sci. 2 (2018) 10, https://doi.org/10.3390/jcs2010010.